

Surface Topography Modeling and Analysis of Camshaft Generated by Swing Grinding Process

Guochao Li (✉ liguochaolaile@126.com)

Jiangsu University of Science and Technology <https://orcid.org/0000-0001-6917-084X>

Jie Lu

Jiangsu University of Science and Technology

Honggen Zhou

Jiangsu University of Science and Technology

Baojiang Dong

Jiangsu University of Science and Technology

Jianzhi Chen

Jiangsu University of Science and Technology

Li Sun

Jiangsu University of Science and Technology

Fei Yang

Shaanxi Diesel Engine Heavy Industry co., Ltd., Xingping

Research Article

Keywords: Swing grinding, Camshaft, Surface topography, Modelling and simulation, Roughness

Posted Date: March 3rd, 2022

DOI: <https://doi.org/10.21203/rs.3.rs-1407584/v1>

License:   This work is licensed under a Creative Commons Attribution 4.0 International License.

[Read Full License](#)

Surface Topography Modeling and Analysis of Camshaft Generated by Swing Grinding Process

Guochao Li^{1,*}, Jie Lu^a, Honggen Zhou¹, Baojiang Dong¹, Jianzhi Chen¹, Li Sun^{1,2}, Fei Yang³

¹ School of Mechanical Engineering, Jiangsu University of Science and Technology, Zhenjiang 212003, China;

² Department of Automation, Rocket Force University of Engineering, Xi'an 710025, PR China

³ Shaanxi Diesel Engine Heavy Industry co., Ltd., Xingping 713100, China

Abstract. In conventional grinding (CG), camshafts with wide profiles suffer from poor quality and low efficiency because the large contact area between the grinding wheel and camshaft profile limits the diffusion of grinding temperature, leading to burn defects. Swing grinding (SG) can mitigate these problems as it involves a reciprocating motion along the axis of the grinding wheel; however, the lack of understanding of machined surface topography has restricted its application. Therefore, in this study, a surface topography prediction model was proposed based on the distribution, shape, and trajectory of grains. The model was verified through experiments, and the mean error was 10.2% for Rax and 3.8% for Ray ; the roughness along the grinding direction was Rax , and the roughness along the vertical grinding direction was Ray . Compared to CG, SG has a 8% lower Rax . The influence of the wheel speed and feed rate in SG is consistent with that in CG. Rax exhibited a periodic trend with an increase in the swing amplitude and a monotonically decreasing trend with an increase in the swing frequency. The variation trend of Ray with the swing amplitude was the same as that of Rax . Furthermore, Ray exhibited a nonlinear increasing trend with an increase in swing frequency. Considering the processing and practical application of camshafts, the swing amplitude should be within 4 mm, the swing frequency should be within 3 Hz, the grinding wheel speed should be large, and the feed rate should be small.

Keywords: Swing grinding; Camshaft; Surface topography; Modelling and simulation; Roughness

* Corresponding authors: Guochao Li

liguochaolaile@126.com

1. Introduction

Processing methods include turning, milling, EDM[1] and grinding, etc. The camshaft is a key component of a marine diesel engine. Rapid wear can occur easily under high temperatures and impact loads during operation. A high-precision and high-quality camshaft profile is key to ensuring a long service life of camshafts. Conventional grinding (CG) can easily cause grinding burns and out-of-tolerance shapes and positions when machining camshafts with a wide profile. Swing grinding (SG) can ensure high-efficiency and high-quality machining of camshafts with a wide profile by using a narrow grinding wheel, increasing the periodic reciprocating movement along the axial direction of the grinding wheel and making the feed movement along the radial direction of the grinding wheel.

At present, the modelling methods of grinding surface topography can be roughly divided into three categories: empirical modeling, theoretical modeling, and finite element modeling.

Empirical modelling primarily comprises surface topography modelling methods based on data analysis and machine learning; this is because these methods are simple and easy to operate, have high prediction accuracy and strong self-learning abilities[2]. However, these methods have the disadvantages of limited prediction range and the significant influence of human factors[3]-[5]. Furthermore, marine diesel camshafts are produced in small batches, with few experimental samples. In the finite element simulation method, simple models can be used to replace complex problems and solve them. Complex grinding mechanisms involved in the grinding process are difficult to observe with the naked eye or even with instruments. Most scholars have studied surface topography by grinding single abrasive grains[6]. Li et al. [7]studied the formation mechanism of surface and subsurface cracks through a finite element grinding simulation of single abrasive grains. Zhou et al. [8]simulated the grinding of ceramic materials using finite elements and determined the surface roughness of workpiece grinding through displacement change. Grinding is the cutting process of thousands of abrasive grains on the surface of a workpiece; therefore, it is

insufficient to analyse only single abrasive grains.

The current mainstream prediction method involves theoretical modelling as it ensures a better understanding of the difference in the surface topography caused by the interaction between the grinding wheel and workpiece, contact method and grinding characteristics. The general theoretical modelling process can be divided into two steps[9]: in the first step, a surface topography model of the grinding wheel is established; in the second step, according to the kinematic relationship between the grinding wheel and workpiece, combined with the grinding principle, the grinding surface topography is predicted. The movement of the grinding wheel in the grinding zone is closely related to the formation of the surface[10]. The entire grinding process is random due to the random shape and distribution of abrasive grains.

Two methods are commonly used to perform the first step. In one of the methods, it is assumed that the abrasive grains have a simple geometric shape and are randomly distributed; subsequently, a surface model of the grinding wheel is established[11][12]. In the other method, a measuring instrument is used to measure and reconstruct the surface topography of the grinding wheel; Ding et al. [13]used this method to reconstruct the surface topography of a grinding wheel through FFT and Johnson transformation. Dai et al.[14] reconstructed the surface topology of a single-textured CBN wheel using the Johnson transform and its inverse transform.

The workpiece surface topography is generated by establishing a grinding material removal mechanism. Liu et al. [15]presented the development of models that describe the surface-generation process for microend milling. Chen et al. [16] studied the generation method of grinding surface topography and simulated the grinding force during the grinding process. Wen et al. [17]assumed that the abrasive grain height obeyed a Gaussian distribution and established a motion trajectory equation to simulate the surface topography of the workpiece. Nguyen et al. [18]established an abrasive grain cutting trajectory and mapped it to the workpiece surface coordinate system to obtain the three-dimensional topography of the ground workpiece surface.

At present, the formation mechanism of the surface morphology of SG and the influence

of the grinding process parameters on the formation of the surface morphology need further investigation. SG motions are similar to that of ultrasonic vibration grinding (UVG). UVG is a machining method that combines CG with Ultrasonic Vibration (UV) machining; it is suitable for machining brittle and hard materials and creating tiny holes.

Li et al. [19] used a scanner to observe UVG and used CG to produce different wear debris shapes. Peng et al. [20] arrived at a similar conclusion. In the past decades, undeformed cutting thickness has been used to evaluate grinding performance [21]. Li et al. [22] used a Doppler vibrometer to verify that tiny radial vibrations were the primary reason for the formation of short wear debris. Wang et al. [23] studied the morphology of diamond grinding wheels, with the results showing that the steady-state process area of sapphire in the elliptical ultrasonic assisted grinding (EUAG) process was longer than that in the CG process. Zhou et al. [24] found that the matching phase difference (MPD) can be used to characterise the matching relationship between the ultrasonic vibration parameters and grinding process parameters. Sun et al. [25] studied UG cylindrical grinding and found that the micro-spiral chip pocket micro-grinder (MAT-HCP) had good chip evacuation performance and improved wear resistance. Yin et al. [26] discovered a new method for measuring wheel wear and predicting the surface roughness. Zhu et al. [27] analysed the electrochemical drilling and grinding process and conducted a simulation study to elucidate the role of the ultrasonic-assisted electrochemical drill-grinding (UAECDG) process in improving the machining accuracy. Zhou et al. [28] found that applying axial vibration increased the number of dynamically active grains, produced a uniform undeformed chip thickness, and reduced the surface roughness.

Considering the complex grinding trajectory, the surface topography generated by SG was modelled and analysed in this study. This article is structured as follows. First, the modelling process of the model is introduced, including the working principle of SG and the simulation process of the surface topography of the grinding wheel and workpiece. Second, two-dimensional evaluation parameters are selected to characterise the surface topography of the SG, i.e., the roughness along the grinding direction Rax and the roughness along the

vertical grinding direction R_{ay} . Subsequently, the influence of the conventional parameters and two-dimensional swing parameters on the surface topography and surface roughness in SG is discussed.

2. Surface Topography Modelling and Verification

2.1 Principle of SG

Camshaft swing grinding is based on CG, in which a low-frequency and high-amplitude swing is applied along the axis of the grinding wheel to realise cylindrical grinding. Fig. 1(a) shows the working principle of SG. In the coordinate system used in this study, the x -axis is along the direction of movement of the camshaft feed, the y -axis is parallel to the axis of the grinding wheel, and the z -axis is along the direction of movement of the grinding wheel frame. The grinding depth is a_p ; the wheel rotation speed is n_s ; the wheel speed is V_s ; the radius of the grinding wheel is R ; the angular velocity of the grinding wheel is ω_s ; the radius of the grains is R_g . A and f are the swing amplitude and frequency, respectively, and the feed rate is V_w . Fig. 1(b) shows the grinding trajectory of the abrasive grains during CG, and Fig. 1(c) shows the grinding trajectory of the abrasive grains during SG.

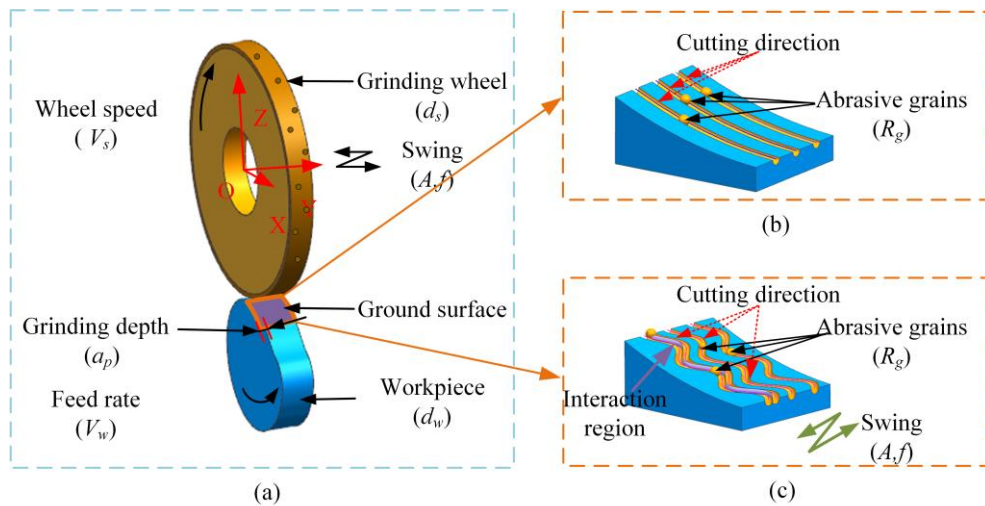


Fig. 1. Schematic diagram of grinding: (a) swing processing principle, (b) grain trajectories during CG, and (c) grain trajectories during SG

The grinding mechanism of SG is significantly different from that of CG; the grinding topography of the machined surface is also different. Therefore, it is necessary to study the

formation mechanism of the SG surfaces. The trajectory of a single abrasive particle is described below. Assuming that the grinding start time is $t_0=0$ s, the initial phase angle is 0. The abrasive grains at the contact point of the grinding wheel workpiece are considered the starting point. In this study, cylindrical grinding was simplified to surface grinding. Thus, the trajectory equation of a single abrasive grain in SG is as follows:

$$\begin{cases} x(t) = R\cos\left(\omega_s t - \frac{\pi}{2}\right) \pm V_w t \\ y(t) = A\sin\left(2\pi f t + \frac{\pi}{2}\right) \\ z(t) = R\sin\left(\omega_s t + \frac{\pi}{2}\right) + R + R_g - a_p \end{cases} \quad (1)$$

The " \pm " in $x(t)$ is taken as "-" when the grinding is performed downwards and "+" when the grinding is performed backwards. In the equation above, R is the radius of the grinding wheel (mm), ω_s is the angular velocity of the grinding wheel (rad/s), V_w is the workpiece feed rate (mm/min), A is the swing amplitude (mm), f is the swing frequency (Hz), R_g is the grain radius (mm), and a_p is the grinding depth (μm).

2.2 Modelling of wheel topography

The geometry and distribution of the grains on the grinding wheel significantly affected the surface roughness of the workpiece. The grinding surface was modelled based on the trajectory of the grains on the grinding wheel surface. However, the actual grains were irregular in shape. Considering that there was a large negative rake angle during the grinding process, the shape of the grains was assumed to be spherical[29]. Furthermore, the following assumptions were made regarding the grinding process and the grains:

(1) The grains on the surface of the grinding wheel were spherical. The spatial distribution and size of the grains were uniform, and their height was Gaussian.

(2) In theoretical research, the influence of elastic deformation, plastic deformation and grinding heat during the grinding process is not considered. Therefore, in this study, the material was assumed to be an ideal metal.

(3) The swing amplitude and frequency were stable during the SG process.

(4) In theoretical research, for the convenience of calculation, it is assumed that when

the grinding wheel is in contact with the workpiece, the grinding time is $t = 0$ s, and the initial phase angle of swing grinding is 0.

Fig. 2 shows the step analysis of the grain-modelling process on the surface of the grinding wheel. In the fig.2, m is the circumferential direction of the grinding wheel, and n is the direction of the axis of the grinding wheel.

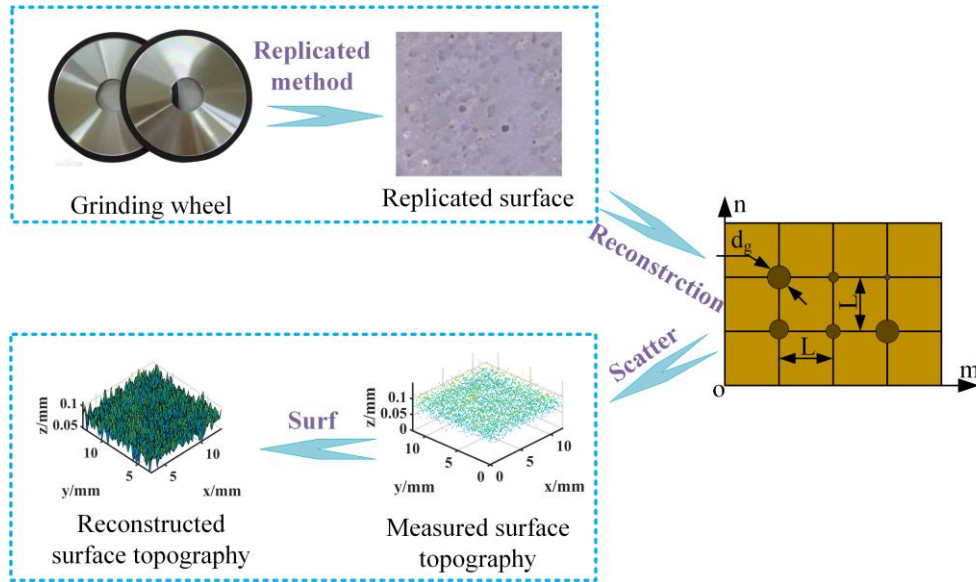


Fig. 2. Modelling process of grains on the surface of the grinding wheel

The distance L between the grains and the position of each grain can be expressed by the following equation:

$$\{G_{i,j}\} = \begin{Bmatrix} G_{i,j}^x \\ G_{i,j}^y \end{Bmatrix} = \begin{Bmatrix} G_{0,0}^x + i \cdot \Delta x \\ G_{0,0}^y + j \cdot \Delta y \end{Bmatrix} \quad (2)$$

In the equation above, $G_{(i,j)}$ represents the position of the centre of each grain on the plane. $G_{0,0}^x$ and $G_{0,0}^y$ indicate the positions of the centre of the first grain on the x -axis and y -axis, respectively. In addition, $\Delta x = \Delta y = L$. The equation used for calculating the grain spacing L is as follows:

$$L = 137.9M^{-1.4} \sqrt{\frac{\pi}{32-S}} \quad (3)$$

In the equation above, M is the grain mesh number, $S = 32 - (V_g/2)$ is the grinding wheel structure parameter, and V_g (%) is the grain concentration.

The geometry and distribution of the grains on the grinding wheel significantly affected the surface morphology of the workpiece. The grains were characterised by their size and height. It was assumed that the surface of the grinding wheel was composed of several spherical grains with a diameter of d_g . The maximum grain diameter, d_{gmax} , and average grain diameter, d_{gavg} , were calculated using the following equations[30]:

$$d_{gmax} = 15.2M^{-1} \quad (4)$$

$$d_{gavg} = 68M^{-1.4} \quad (5)$$

The diameter d_g and height hi of the grains were used to approximate the Gaussian distributions $P(dg)$ and $P(hi)$ [31]. The two equations used are as follows:

$$P(d_g) = \frac{A_1}{\sigma\sqrt{2\pi}} \exp \left[-\frac{1}{8} \left(\frac{d_g - d_{davg}}{\sigma} \right)^2 \right] \quad (6)$$

$$P(hi) = \frac{1}{\sigma\sqrt{2\pi}} \exp \left(-\frac{(h_i - \mu)^2}{2\sigma^2} \right) \quad (7)$$

In eq (6) and (7), the standard deviation is $\sigma = (d_{gmax} - d_{gavg})/3$, and the average is $\mu = d_{gmax}$.

There are many cutting points on spherical grains. In this study, the highest point of the grains was selected as the cutting point. A bilinear interpolation algorithm was used to refine the grids further, and each grain was labelled. The row is denoted by m , the column by n , and the height of the grain by h_{mn} ; the row number, column number and height are registered in the matrix $H(m * n)$.

2.3 Establishment of abrasive trajectories

The generation of the surface topography of the workpiece was similar to that of the grinding wheel surface. Extraction of the remaining grinding height was crucial for evaluating the workpiece surface topography generation, as shown in Fig. 3.

$$\begin{cases} x_m^n(t) = R \cos\left(\omega_s \left(t + \frac{L}{V_s}\right) - \frac{\pi}{2}\right) + V_w \left(t + \frac{L(m-1)}{V_s}\right) \\ y_m^n(t) = A \sin\left(2\pi f \left(t + \frac{L(m-1)}{V_s}\right) + \frac{\pi}{2}\right) + L(m-1) \\ z_m^n(t) = R \sin\left(\omega_s \left(t + \frac{L(m-1)}{V_s}\right) + \frac{\pi}{2}\right) + R + H(m, n) - a_p \end{cases} \quad (10)$$

The same sampling point on the workpiece surface was ground by abrasive grains of different heights because the speed of the grinding wheel was much greater than that of the workpiece. In this study, the grinding sampling point map of the abrasive grain G on the workpiece surface is denoted by P . The grinding point map P was ground thrice, and the grinding points were P_1 , P_2 , and P_3 . The abrasive grain heights were $H_{G1} > H_{G2} > H_{G3}$. The remaining heights of the workpiece surface were $W_{G3} > W_{G2} > W_{G1}$. The final remaining topography on the actual workpiece surface was determined using the grit G_1 . Therefore, the minimum values in the W_G matrix were compared.

$$W(i, j) = \min(W_G(i, j)) \quad (11)$$

Fig. 4 shows the simulation diagram of the surface topography of the grinding wheel when the mesh of the grains was $M=120$. The simulation generation process was controlled by the grinding wheel mesh M , distance between the grains L , mean value μ and variance σ .

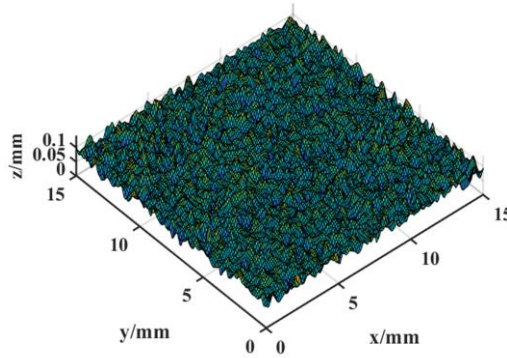


Fig. 4. Simulation diagram of the surface topography of the grinding wheel

2.4 Estimation of surface topography characterization

The grinding surface topography map is composed of a matrix, and different characterisation parameters are evaluated according to the different characterisation concept equations to quantify the surface topography. The one-dimensional roughness parameter, Ra , is often used to quantify the surface topography. In the CG process, only the rotating

movement of the grinding wheel and the workpiece feeding movement are present; however, in SG, which is based on CG, a simple harmonic motion is added along the y -axis. In this study, two-dimensional surface roughness, Rax and Ray , were selected as the characterisation parameters of the SG surface topography. Rax was the cross-sectional roughness along the grinding direction, and Ray was the cross-sectional roughness perpendicular to the grinding direction. Fig. 5 shows the topography of the grinding wheel and grinding camshaft surface. Fig. 5(a) shows the grinding texture of the camshaft surface, and Fig. 5(b) is a partially enlarged view of Fig. 5(a). The surface topography in Fig. 5(b) was determined using $V_s=80$ m/s, $V_w=1800$ mm/min, $a_p=3$ μ m, $A=2$ mm and $f=20$ Hz. Fig. 6 shows the cross-sectional profile along the grinding direction and perpendicular to the workpiece grinding direction.

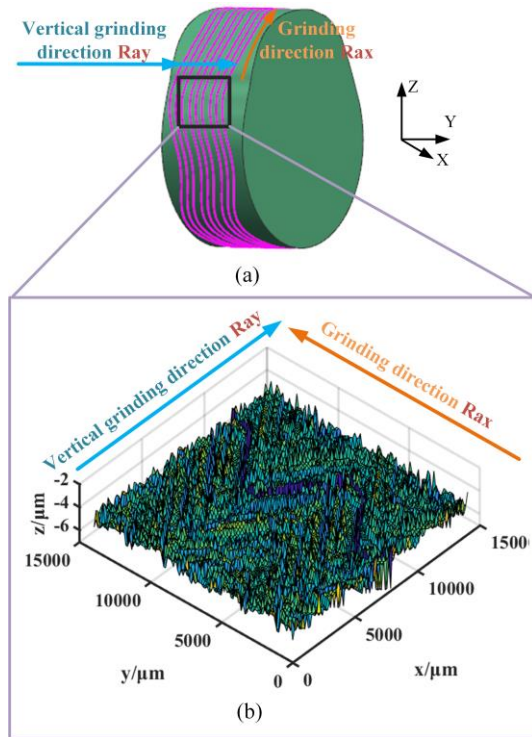


Fig. 5. Simulation diagram of the surface topography of SG ((a) camshaft surface grinding texture, (b) partial magnification)

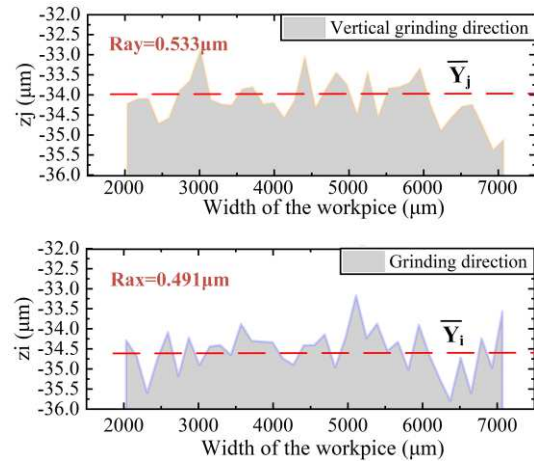


Fig. 6. Cross-sectional surface profile along the workpiece grinding direction and perpendicular to the grinding direction

The calculation process of the surface roughness R_a is as follows:

- 1) Evaluate \bar{Y} such that the upper and lower areas of the line are equal; \bar{Y} is the average value of all z_i or z_j values, and N is the number of data points within the sampling length of

the workpiece.

$$\bar{Y}_l = \frac{1}{N} \sum_{i=1}^N z_i \text{ or } \bar{Y}_j = \frac{1}{N} \sum_{j=1}^N z_j \quad (12)$$

2) Calculate the average roughness value of the intercepted section (for example, the m -th section):

$$\overline{R_{m_i}} = \frac{1}{N} \sum_{Q=1}^N |z_i - \bar{Y}_l| \text{ or } \overline{R_{m_j}} = \frac{1}{N} \sum_{Q=1}^N |z_j - \bar{Y}_j| \quad (13)$$

The total average roughness of the workpiece can be obtained by averaging the individual R_m values and dividing by the total number of rows; this is referred to as the average surface roughness.

$$R_{ax} = \frac{1}{i} \sum_{m=1}^i \overline{R_{m_i}} \text{ or } R_{ay} = \frac{1}{j} \sum_{m=1}^j \overline{R_{m_j}} \quad (14)$$

In the equation above, i and j are the number of data points along the grinding direction and perpendicular to the grinding direction, respectively. In Fig. 5, R_{ax} is $0.491\mu\text{m}$, and R_{ay} is $0.533\mu\text{m}$. Fig. 7 is the flow chart of the surface topography modeling of SG.

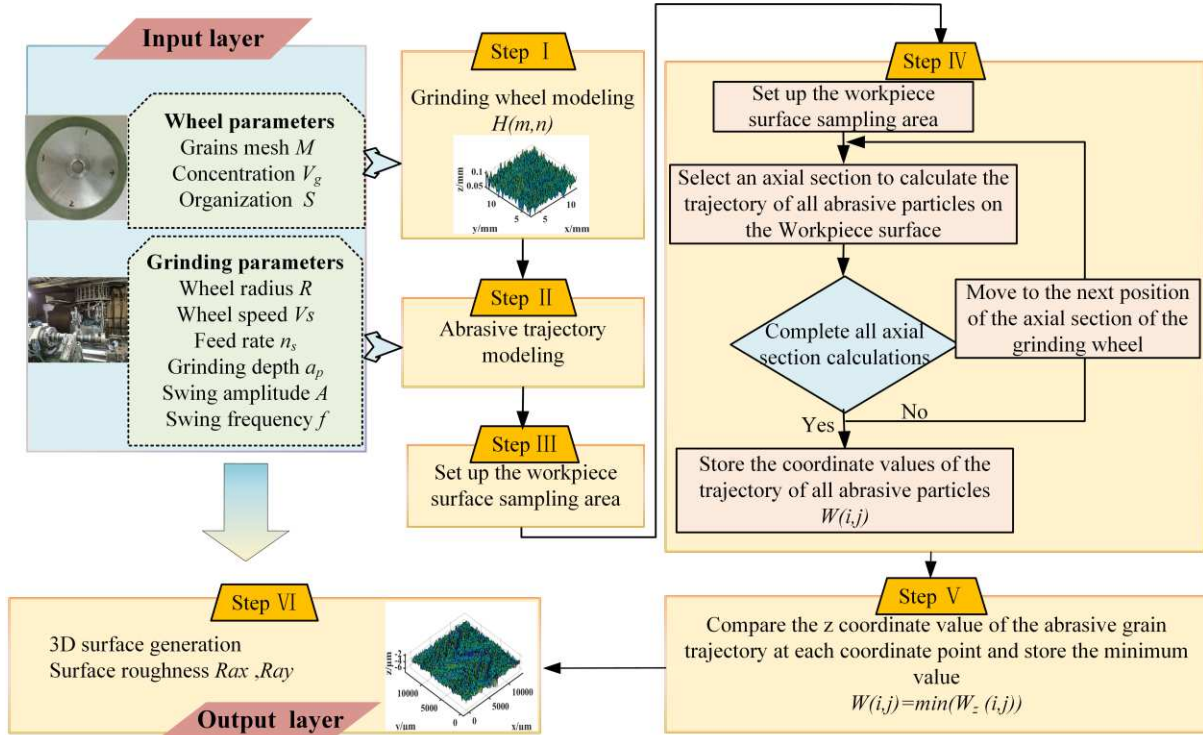


Fig. 7. Flow chart of modelling and simulation of the SG surface topography

2.5 Experimental verification

All the grinding experiments were performed on a CNC grinding machine to verify the accuracy of the simulation. A V-CBN ($280 \times 52 \times 100 \times 5 \times 50$) grinding wheel was used in the experiment. CBN grinding wheels exhibit good self-grinding properties, which can improve the grinding performance and reduce the grinding heat and grinding force. This method is suitable for grinding both hard and brittle materials. The surface topography measuring instrument used in the experiment was highly accurate, as it could measure micron-scale topography. The experimental arrangement and the shape measurement process of the finished product are shown in Fig. 8. The grinding process parameters used in the experiments are listed in Table. 1.

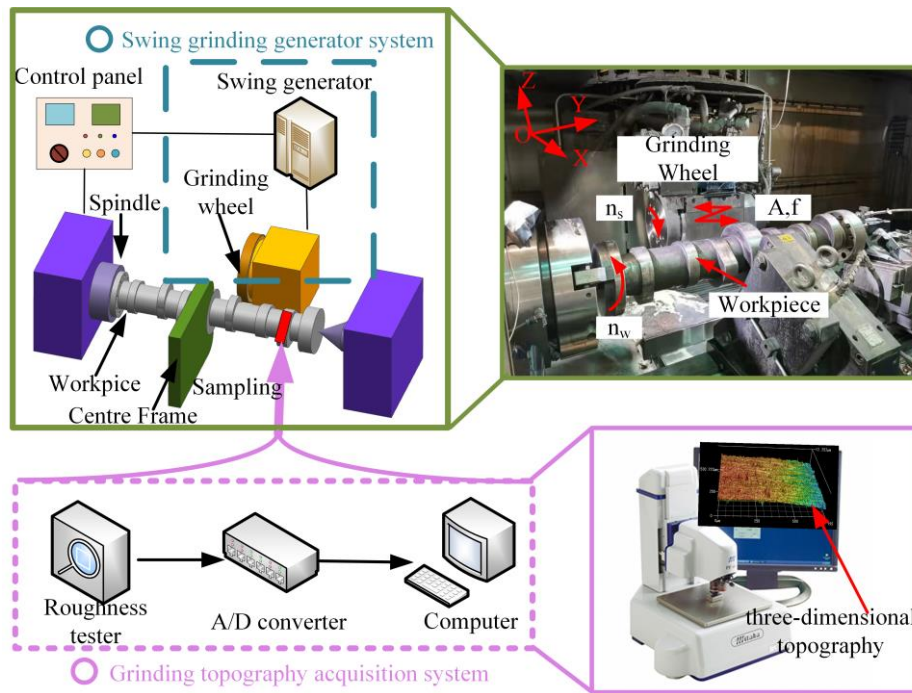


Fig. 8. Layout of the experimental and measurement devices

Table. 1. Grinding experiment processing parameters

Parameter Type	Parameter name	Parameter value
Wheel parameters	Grinding wheel mesh M	120
	Wheel radius R (mm)	140
Conventional parameters	Wheel speed V_s (m/s)	50, 60, 65
	Feed rate V_w (mm/min)	1800
Swing parameters	Swing amplitude A (mm)	0, 2

CG is a special case of SG with swing parameters $A=0$ mm and $f=0$ Hz. Table 2 presents the laser scanning microscope measurement image and grinding topography simulation image obtained from the CG and SG camshaft surface tests. The three wheel speeds were $V_{s1} = 50$ m/s, $V_{s2} = 60$ m/s and $V_{s3} = 65$ m/s. The other parameters were $M = 120$, $R = 140$ mm, $V_w = 1800$ mm/min, $a_p = 3$ μ m, $A_1 = 0$ mm, $A_2 = 2$ mm, $f_1 = 0$ Hz and $f_2 = 2$ Hz. As shown in Fig. 9, under the same material removal rate, the roughness of SG was reduced by 8% compared with that of CG. Table. 2 is the comparison of shape measurement diagram and simulation diagram of CG and SG at different V_s .

The wheel speed played a significant role in the X-direction, and the swing parameters played a significant role in the Y-direction. The grinding rate in the X-direction was greater than that in the Y-direction, which led to a more obvious interference of abrasive grains in the X-direction and repeated grinding. As shown in Fig. 9, based on the comparison between the roughness values of the SG experiment and simulation, the average errors of the Rax and Ray models were 10.2% and 3.8%, respectively; Rax was larger than Ray . As the texture of CG in the vertical grinding direction was a straight groove, the Ray of CG was 0 μ m.

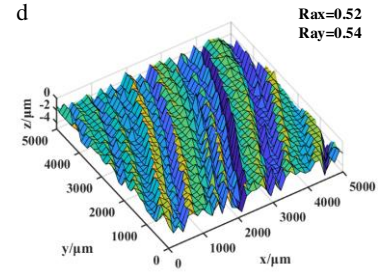
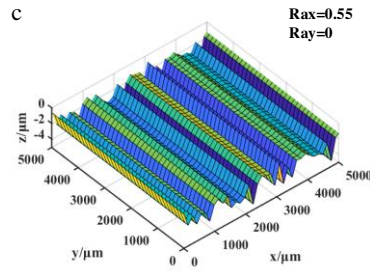
The calculation process primarily involved computing discrete data, which were only applicable to matrix operations. Therefore, to improve the practicability of the algorithm, the calculation procedure was encapsulated in MATLAB software and executed on a PC with the following configurations: processor: Intel(R) Core (TM) i5-10200H; CPU: 2.40 GHz; RAM:16384 MB. The runtime of the program was 1.5 s.

Table. 2. Comparison of shape measurement diagram and simulation diagram of CG and SG at different

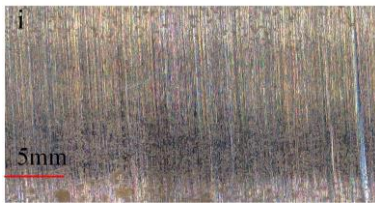
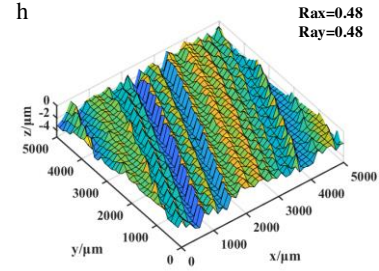
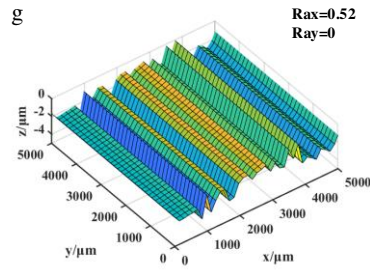
V_s		
V_s (m/s)	$M=120, R=140\text{mm}, V_w=1800\text{mm/min}$	
	CG ($A=0\text{mm}, f=0\text{HZ}$)	SG ($A=2\text{mm}, f=2\text{HZ}$)



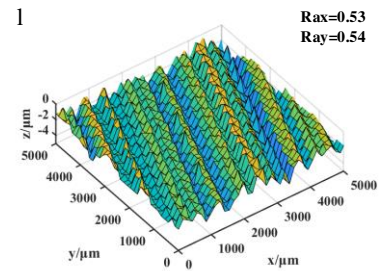
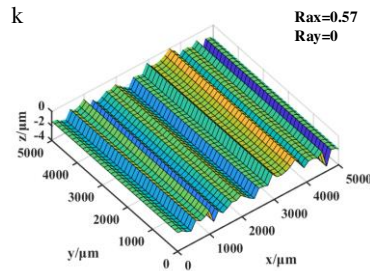
50



60



65



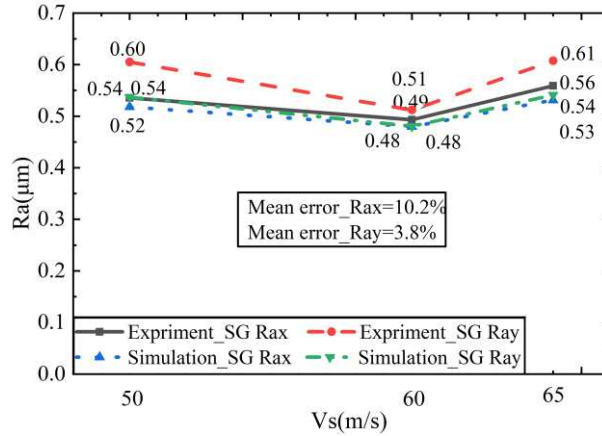


Fig. 9. Comparison of swing grinding experiment and simulation roughness

The prediction model ignores the vibration of the machine tool, wear of the grinding wheel, rigidity of the grinding wheel, and other influencing factors. The vibration of the machine tool causes the grains to deviate from the ideal trajectory during the grinding process. The wear of the grinding wheel also causes a certain deviation in the prediction.

3 Analysis of SG on surface topography

In this section, a single-factor experiment and an orthogonal experiment were selected to analyse the influence law of the established prediction model under different grinding process parameters. The single-factor experiment was designed to control the influence of non-research factors on the experiment, and only one factor affecting the effect indicators was considered for analysing the effects of the influencing factors. An orthogonal experiment was designed to examine the interaction and coupling between the factors and identify the most influential factors and the best combinations to determine the influence of the grinding process parameters on SG.

3.1 Single-factor analysis of SG

Four factors and six levels were selected. R was 140 mm, and M was 120. V_s , V_w , f and A were the influencing factors. Rax and Ray were used as evaluation indicators of surface topography. Table. 3 lists the typical values of the SG grinding process parameters and the value range of the simulation test. Fig. 10 shows the grinding surface topography for different

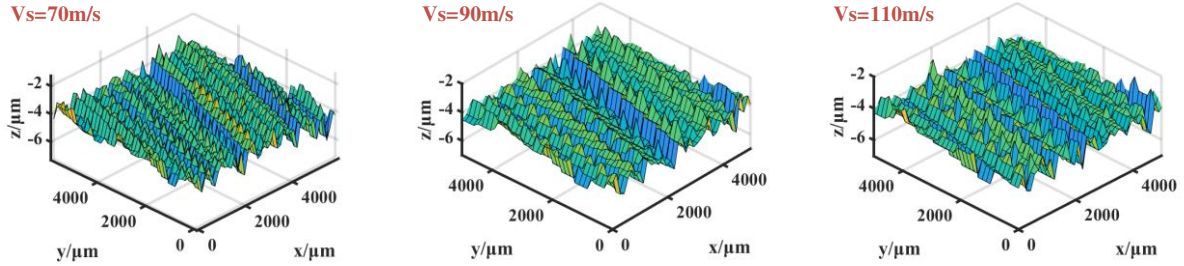
grinding process parameters. Fig. 11 shows the relationship between the SG grinding process parameters and surface roughness.

Table. 3. Typical grinding parameters and simulation value ranges

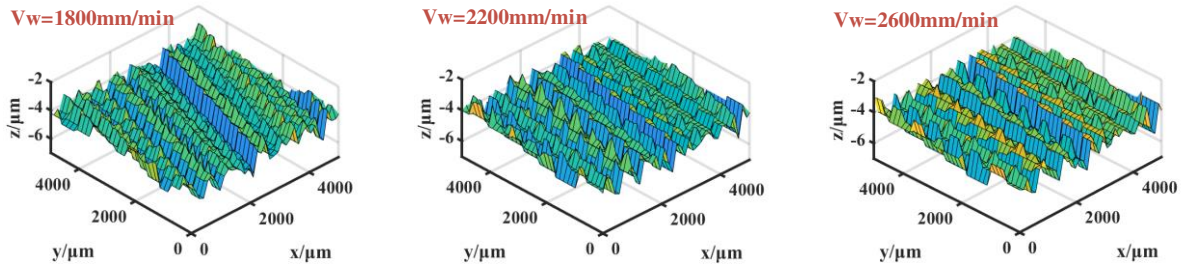
Group	Grinding process parameters	Typical parameters	Simulation value range
Group NO.1	V_s , m/s	80	60, 70, 80, 90, 100, 120
Group NO.2	V_w , mm/min	1800	1800, 2000, 2200, 2400, 2600, 2800
Group NO.3	f , HZ	2	2, 4, 6, 8, 10, 12
Group NO.4	A , mm	2	2, 4, 6, 8, 10, 12

Fig. 10(a) shows that as V_s increased, the surface quality increased, and the surface roughness decreased. Furthermore, when V_s increased, the average thickness of the abrasive particles decreased. Fig. 10(b) shows that as V_w increased, the surface quality decreased, and the surface roughness increased. When V_w was small, the grains acted for a long time in the same working area. The trajectories of the adjacent grains overlapped. Therefore, shallow and narrow grooves were formed on the ground surface, and the ground surface quality was good. When V_w increased, the opposite effect was observed. Fig. 10(c) shows that as f increased, the surface quality increased, and the surface roughness decreased. When the swing frequency was increased, the reciprocating grinding interference per unit grinding time increased, and the surface material of the workpiece became smoother. Fig. 10(d) shows that as A increased, the surface quality increased, and the roughness decreased. The grinding surface roughness had inflection points at $A=6$ and 14 mm. When A was very small, the exercise path of the abrasive surface was relatively small, and the roughness was high. When A was greater than 14 mm, the grinding reciprocating interference effect of the grains on the surface of the workpiece was enhanced, and the roughness was reduced. In the actual processing, the smaller A was, the smaller the impact on the crushing and extraction of grains, and the surface quality improved. With an increase in A , the reciprocating grinding interference of the grains on the workpiece surface increased. The effects of the grinding process parameters on the surface quality are shown in Table. 4. Depending on the relative rate of change

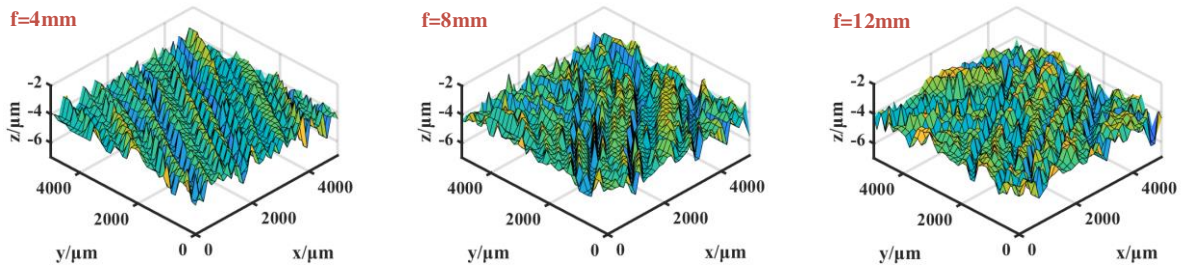
(RR_simulation), the degree of impact of Rax and Ray was sorted, and the sorting of their separate dimensions led to the following results: $V_s > A > f > V_w$ and $A > V_s > f > V_w$. The degrees of influence were similar.



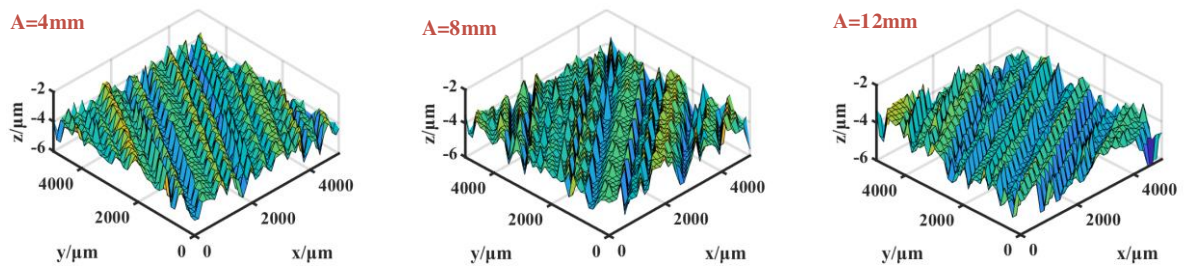
(a) $V_w=1800$ mm/min, $f=2$ HZ, $A=2$ mm



(b) $V_s=80$ m/s, $f=2$ HZ, $A=2$ mm



(c) $V_s=80$ m/s, $V_w=1800$ mm/min, $f=2$ HZ



(d) $V_s=80$ m/s, $V_w=1800$ mm/min, $f=2$ HZ

Fig. 10. Comparison of surface topography under different grinding process parameters.

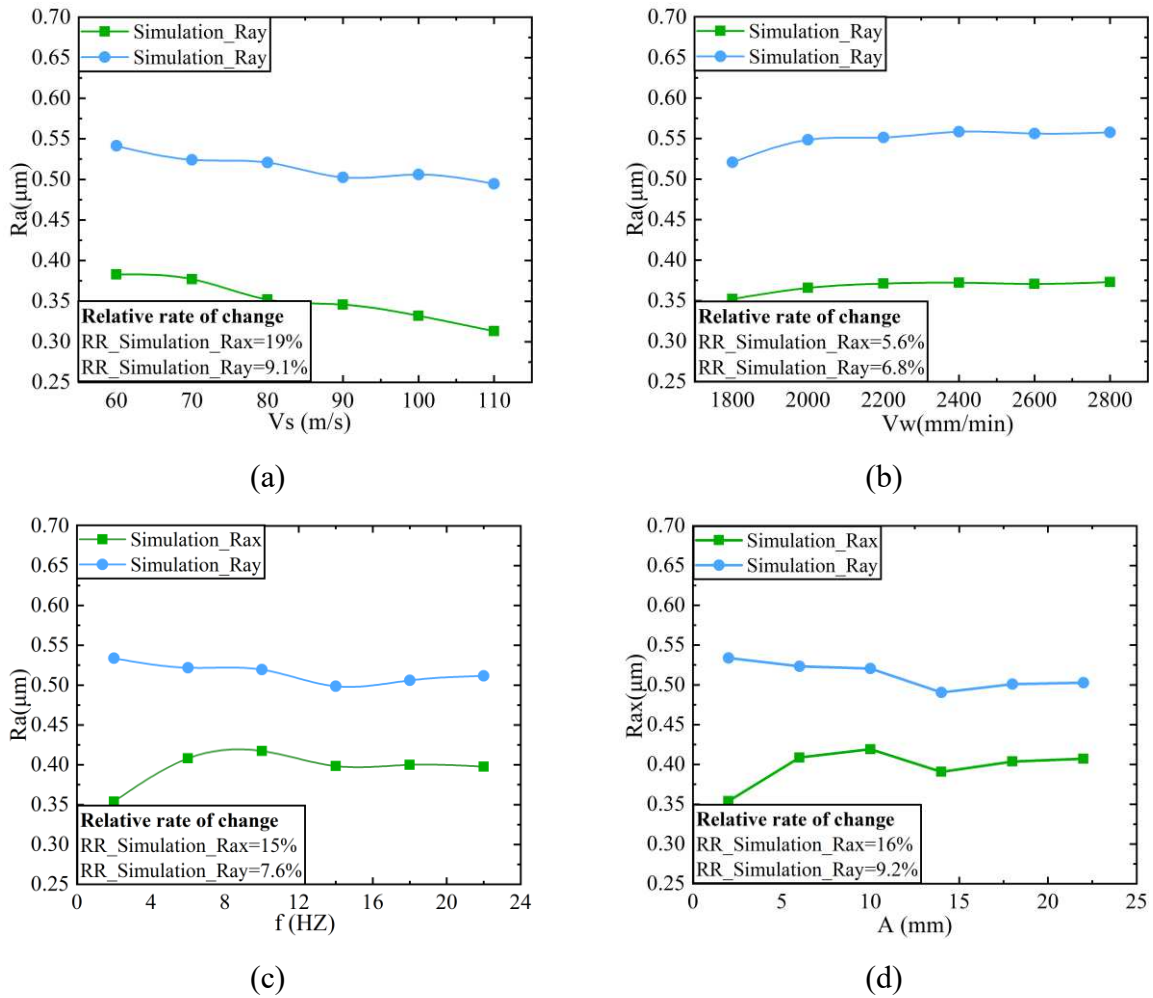


Fig. 11. Single-factor analysis of the surface roughness in SG

Table. 4. Degree of influence of the grinding process parameters on the surface roughness of grinding

the main factor of influence	Degree of influence (+Roughness increase, -Roughness reduce)	
	<i>Rax</i>	<i>Ray</i>
Wheel speed V_s (m/s)	++++	+++
Feed rate V_w (mm/min)	-	-
Swing amplitude A (mm)	+++	++++
Swing frequency f (HZ)	++	+++

The special features of SG are the swing amplitude and swing frequency; therefore, it is necessary to study the two swing parameters. Fig. 12 shows the relationship between the rate of change in roughness with increasing swing frequency and amplitude.

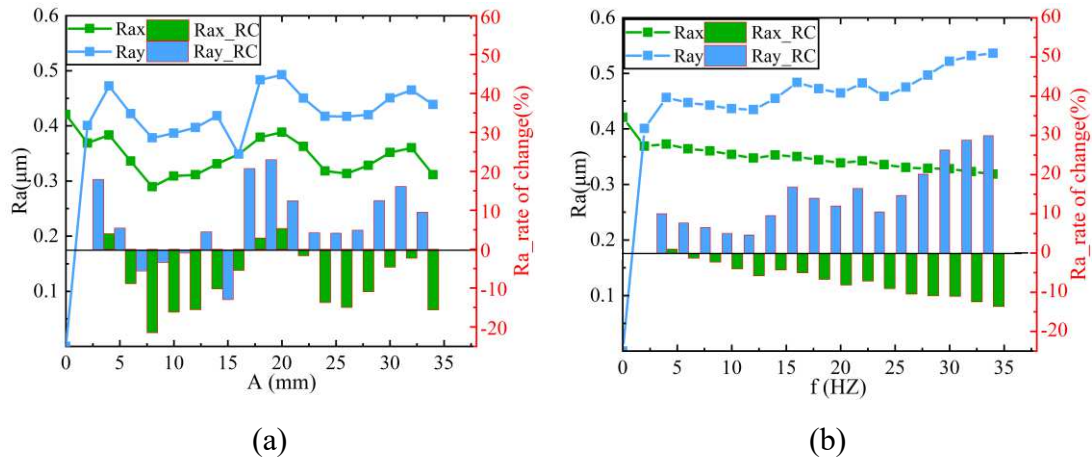


Fig. 12. Relationship between the swing parameters, roughness and roughness change rate ((a) swing amplitude, (b) swing frequency)

In Fig. 12, with an increase in A and f , the rate of change of Rax was -8.3% and -7.0% , respectively (“-” indicates a decrease in roughness, and “+” indicates an increase in roughness). The rate of change of Ray with an increase in A and f was 4.1% and 18% , respectively. A had a significant influence on Rax , and f had a significant influence on Ray . As A increased, changes in both Rax and Ray showed trends similar to those of the cyclical changes. An increase of 6 mm in A resulted in a peak and a low roughness value. With an increase in f , the variation trend of Rax was an approximately monotonically decreasing function, and Ray exhibited a nonlinear increasing trend. When f was greater than 30 Hz, the rates of change of Rax and Ray decreased and gradually tended to be flat.

3.2 Orthogonal experimental analysis of SG

An orthogonal experiment with four factors and three levels was designed to determine the most sensitive factors influencing the ground surface topography. The four factors were V_s , V_w , f and A . Nine sets of simulation experiments were designed. Table. 5 lists the nine sets of experiments. Rax and ray were selected as the evaluation indices of the surface topography.

The results of the orthogonal experiments are presented in Table. 6. At the i^{th} ($i = 1,2,3$) level, the mean roughness Rax was represented by K_i , and the mean roughness Ray was represented by G_i .

According to the orthogonal analysis, the priority order of the influence of the factors on R_{ax} and R_{ay} were V_s, A, f, V_w and A, V_s, f, V_w , respectively. R_{ax} and R_{ay} exhibited similar rankings for the influencing factors.

Table. 5. Simulation orthogonal experimental design (grinding process parameters)

Number	Wheel speed V_s (m/s)	Feed rate V_w (mm/min)	Swing frequency f (time/min)	Swing amplitude A (mm)	R_{ax} (μm)	R_{ay} (μm)
	A1=50	B1=1800	C1=2	D1=2		
	A2=100	B2=2000	C2=6	D2=6		
	A3=150	B3=2200	C3=10	D3=10		
NO.1	A1	B1	C1	D1	0.445	0.546
NO.2	A1	B2	C2	D2	0.468	0.592
NO.3	A1	B3	C3	D3	0.466	0.636
NO.4	A2	B1	C2	D3	0.464	0.545
NO.5	A2	B2	C3	D1	0.439	0.559
NO.6	A2	B3	C1	D2	0.465	0.568
NO.7	A3	B1	C3	D2	0.468	0.585
NO.8	A3	B2	C1	D3	0.435	0.546
NO.9	A3	B3	C2	D1	0.442	0.551

Table. 6. Orthogonal experiment calculation results

K1	1.380	1.377	1.345	1.365	G1	1.774	1.696	1.709	1.768
K2	1.368	1.343	1.374	1.402	G2	1.686	1.704	1.699	1.745
K3	1.345	1.374	1.374	1.326	G3	1.688	1.747	1.767	1.635
k1	0.460	0.459	0.448	0.455	g1	0.591	0.565	0.570	0.589
k2	0.456	0.448	0.458	0.467	g2	0.562	0.568	0.566	0.582
k3	0.448	0.458	0.458	0.442	g3	0.563	0.582	0.589	0.545
R	0.153	0.139	0.144	0.147	R	0.029	0.017	0.023	0.044
Order	1	4	3	2	Order	2	4	3	1
Optimal plan	A3B2C1D3				Optimal plan	A2B1C2D3			

The selection of the optimal surface roughness in SG is shown in Fig. 13. The smallest choice for R_{ax} was A3B2C1D3; $V_s=150$ m/s, $V_w=2000$ mm/min, $f=2$ Hz, $A=10$ mm. The R_{ax} value was $0.435\mu\text{m}$. The smallest choice for r_{ay} was A2B1C2D3; $V_s=100$ m/s, $V_w=1800$ mm/min, $f=6$ Hz, $A=10$ mm. The R_{ax} value was $0.545\mu\text{m}$.

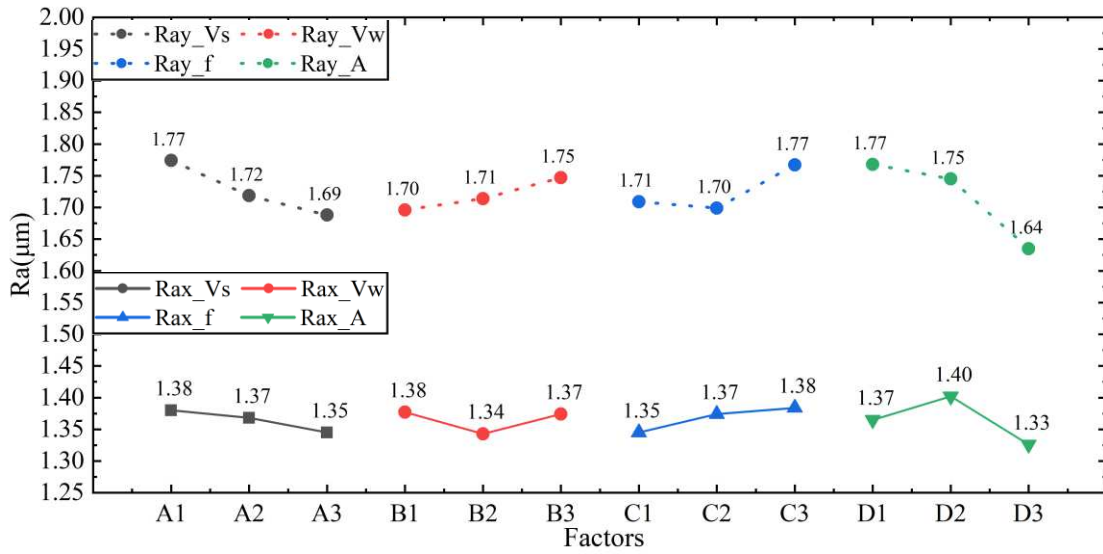


Fig. 13. SG index factors graph

The conclusion of the univariate analysis and orthogonal experimental analysis was that Rax was smaller than Ray . In Fig. 5(a), Rax is along the rotational and working directions of the camshaft. Ray is along the camshaft width direction and camshaft non-working direction. Even if Ray increases, a smaller Rax along the rotation direction of the camshaft is better; this is beneficial for the practical application of the camshaft. According to the swing parameters in Fig. 13, A should be restricted to 4 mm, and f should be restricted to 3 Hz to reduce the vibration error between the grinding wheel and camshaft. Under these conditions, the values of Rax and Ray are slightly smaller and more suitable for the grinding of marine diesel camshaft machining.

4 Conclusions

In this study, a surface topography prediction model of a camshaft generated by SG was developed. The formation mechanism of the swing-grinding surface topography can be analysed using this model. From the results of this study, the following conclusions can be drawn:

(1) The prediction model was accurate and efficient. The two-dimensional evaluation parameters Rax and Ray were appropriate for characterising the surface topography generated by SG. The mean errors of the predictions for Rax and Ray were 10.2% and 3.8%, respectively. The runtime of the simulation test was 1.5 s.

(2) SG resulted in a better surface roughness than CG. Under the same material removal rate, the Rax of SG can be reduced by 8%.

(3) Rax and Ray exhibited different changing laws with changes in the grinding process parameters. The variation in Rax and Ray with conventional parameters of SG was the same as that with conventional parameters of CG. However, Rax and Ray of SG changed periodically with an increase in the swing amplitude. With an increase in the swing frequency, Rax decreased linearly, and Ray increased nonlinearly. The separate dimensions of Rax and Ray were ordered as $V_s > A > f > V_w$ and $A > V_s > f > V_w$, respectively.

(4) Considering that the working surface of the camshaft is a rotating surface, and the volume of the grinding wheel and the camshaft is large, the swing amplitude should be within 4 mm, and the swing frequency should be within 3 Hz to reduce the vibration error.

Author contribution Guochao Li put forward the main analysis ideas for the article, revised the article, and supervised the project. Jie Lu completed the modeling, data analysis and processing and the writing of the thesis. Honggen Zhou provided labor and financial support. Baojiang Dong was responsible for the collation and analysis of the experimental data. Jianzhi Chen, Li Sun, and Fei Yang were responsible for the construction of the experimental equipment.

Funding This work was supported by the National Natural Science Foundation of China (grant number. 51605207), the Natural Science Foundation of Jiangsu Province of China (grant number BK20160563), and General project of natural science research for Institutions of Higher Education of Jiangsu Province of China(21KJB510016).

Data availability The authors declare that they have no competing interests.

Data availability All data generated or analyzed during this study were available by emailing to author. (lujie9319@163.com).

Declarations

Ethical approval The work contains no libellous or unlawful statements, does not infringe on the rights of others or contains material or instructions that might cause harm or injury.

Consent to participate and publication The authors consent to participate. In addition, consent for publication Informed consent was obtained from all individual participants involved in the study.

Conflict of interest The authors declare that they have no conflict of interest.

References

- [1] Mujumdar SS, Curreli D, Kapoor SG, Ruzic D. Modeling of Melt-Pool Formation and Material Removal in Micro-Electrodischarge Machining. *Journal of Manufacturing Science and Engineering, Transactions of the ASME* 2015;137. <https://doi.org/10.1115/1.4029446>.
- [2] Zheng W, Zhou M, Zhou L. Influence of process parameters on surface topography in ultrasonic vibration- assisted end grinding of SiCp/Al composites. *International Journal of Advanced Manufacturing Technology* 2017;91:2347–58. <https://doi.org/10.1007/s00170-016-9931-3>.
- [3] Alao AR, Konneh M. Surface finish prediction models for precision grinding of silicon. *International Journal of Advanced Manufacturing Technology* 2012;58:949–67. <https://doi.org/10.1007/s00170-011-3438-8>.
- [4] Zahedi A, Tawakoli T, Akbari J. Energy aspects and workpiece surface characteristics in ultrasonic-assisted cylindrical grinding of alumina-zirconia ceramics. *International Journal of Machine Tools and Manufacture* 2015;90:16–28. <https://doi.org/10.1016/j.ijmachtools.2014.12.002>.
- [5] Cao X, Lin B, Zhang X. A study on grinding surface waviness of woven ceramic matrix composites. *Applied Surface Science* 2013;270:503–12. <https://doi.org/10.1016/j.apsusc.2013.01.069>.
- [6] Jiang JL, Ge PQ, Bi WB, Zhang L, Wang DX, Zhang Y. 2D/3D ground surface topography modeling considering dressing and wear effects in grinding process. *International Journal of Machine Tools and Manufacture* 2013;74:29–40. <https://doi.org/10.1016/j.ijmachtools.2013.07.002>.

-
- [7] Zhou H, Ding W, Liu C. Material removal mechanism of PTMCs in high-speed grinding when considering consecutive action of two abrasive grains. *International Journal of Advanced Manufacturing Technology* 2019;100:153–65. <https://doi.org/10.1007/s00170-018-2685-3>.
- [8] Li B, Ni J, Yang J, Liang SY. Study on high-speed grinding mechanisms for quality and process efficiency. *International Journal of Advanced Manufacturing Technology* 2014;70:813–9. <https://doi.org/10.1007/s00170-013-5297-y>.
- [9] Zhou H, Ding W, Liu C. Material removal mechanism of PTMCs in high-speed grinding when considering consecutive action of two abrasive grains. *International Journal of Advanced Manufacturing Technology* 2019;100:153–65. <https://doi.org/10.1007/s00170-018-2685-3>.
- [10] Hecker RL, Ramoneda IM, Liang SY. Analysis of wheel topography and grit force for grinding process modeling. *Journal of Manufacturing Processes* 2003;5:13–23. [https://doi.org/10.1016/S1526-6125\(03\)70036-X](https://doi.org/10.1016/S1526-6125(03)70036-X).
- [11] Chen H, Tang J, Shao W, Zhao B. An investigation on surface functional parameters in ultrasonic-assisted grinding of soft steel. *International Journal of Advanced Manufacturing Technology* 2018;97:2697–702. <https://doi.org/10.1007/s00170-018-2164-x>.
- [12] Cooper WL, Lavine AS. *Grinding Process Size Effect and Kinematics Numerical Analysis*. 2000.
- [13] Ding W, Dai C, Yu T, Xu J, Fu Y. Grinding performance of textured monolayer CBN wheels: Undeformed chip thickness nonuniformity modeling and ground surface topography prediction. *International Journal of Machine Tools and Manufacture* 2017;122:66–80. <https://doi.org/10.1016/j.ijmachtools.2017.05.006>.
- [14] Dai C, Yin Z, Ding W, Zhu Y. Grinding force and energy modeling of textured monolayer CBN wheels considering undeformed chip thickness nonuniformity. *International Journal of Mechanical Sciences* 2019;157–158:221–30. <https://doi.org/10.1016/j.ijmecsci.2019.04.046>.

-
- [15]Liu X, DeVor RE, Kapoor SG. Model-based analysis of the surface generation in microendmilling - Part I: Model development. *Journal of Manufacturing Science and Engineering, Transactions of the ASME* 2007;129:453–60. <https://doi.org/10.1115/1.2716705>.
- [16]Chen X, Brian Rowe W. 0890-6955(96)00117-4 ANALYSIS AND SIMULATION OF THE GRINDING PROCESS. PART II: MECHANICS OF GRINDING. vol. 36. 1996.
- [17]Wen XN. Modeling and predicting surface roughness for the grinding process. *Applied Mechanics and Materials*, vol. 599–601, Trans Tech Publications Ltd; 2014, p. 622–5. <https://doi.org/10.4028/www.scientific.net/AMM.599-601.622>.
- [18]Nguyen DT, Yin S, Tang Q, Son PX, Duc LA. Online monitoring of surface roughness and grinding wheel wear when grinding Ti-6Al-4V titanium alloy using ANFIS-GPR hybrid algorithm and Taguchi analysis. *Precision Engineering* 2019;55:275–92. <https://doi.org/10.1016/j.precisioneng.2018.09.018>.
- [19]Li S, Wu Y, Nomura M. Effect of grinding wheel ultrasonic vibration on chip formation in surface grinding of Inconel 718. *International Journal of Advanced Manufacturing Technology* 2016;86:1113–25. <https://doi.org/10.1007/s00170-015-8149-0>.
- [20]Peng Y, Liang Z, Wu Y, Guo Y, Wang C. Characteristics of chip generation by vertical elliptic ultrasonic vibration-assisted grinding of brittle materials. *International Journal of Advanced Manufacturing Technology* 2012;62:563–8. <https://doi.org/10.1007/s00170-011-3839-8>.
- [21]Zahedi A, Tawakoli T, Akbari J. Energy aspects and workpiece surface characteristics in ultrasonic-assisted cylindrical grinding of alumina-zirconia ceramics. *International Journal of Machine Tools and Manufacture* 2015;90:16–28. <https://doi.org/10.1016/j.ijmactools.2014.12.002>.
- [22]Li C, Zhang F, Meng B, Liu L, Rao X. Material removal mechanism and grinding force modelling of ultrasonic vibration assisted grinding for SiC ceramics. *Ceramics International* 2017;43:2981–93. <https://doi.org/10.1016/j.ceramint.2016.11.066>.
- [23]Wang Q, Zhao W, Liang Z, Wang X, Zhou T, Wu Y, et al. Investigation of diamond wheel

-
- topography in Elliptical Ultrasonic Assisted Grinding (EUAG) of monocrystal sapphire using fractal analysis method. *Ultrasonics* 2018;84:87–95. <https://doi.org/10.1016/j.ultras.2017.10.012>.
- [24] Zhou W, Tang J, Shao W. Modelling of surface texture and parameters matching considering the interaction of multiple rotation cycles in ultrasonic assisted grinding. *International Journal of Mechanical Sciences* 2020;166. <https://doi.org/10.1016/j.ijmecsci.2019.105246>.
- [25] Sun Y, Su Z, Jin L, Gong Y, Ba D, Yin G, et al. Modelling and analysis of micro-grinding surface generation of hard brittle material machined by micro abrasive tools with helical chip pocket. *Journal of Materials Processing Technology* 2021;297. <https://doi.org/10.1016/j.jmatprotec.2021.117242>.
- [26] Yin S, Nguyen DT, Chen FJ, Tang Q, Duc LA. Application of compressed air in the online monitoring of surface roughness and grinding wheel wear when grinding Ti-6Al-4V titanium alloy. *International Journal of Advanced Manufacturing Technology* 2019;101:1315–31. <https://doi.org/10.1007/s00170-018-2909-6>.
- [27] Zhu X, Liu Y, Zhang J, Wang K, Kong H. Ultrasonic-assisted electrochemical drill-grinding of small holes with high-quality. *Journal of Advanced Research* 2020;23:151–61. <https://doi.org/10.1016/j.jare.2020.02.010>.
- [28] Zhou W, Tang J, Chen H, Shao W. A comprehensive investigation of surface generation and material removal characteristics in ultrasonic vibration assisted grinding. *International Journal of Mechanical Sciences* 2019;156:14–30. <https://doi.org/10.1016/j.ijmecsci.2019.03.026>.
- [29] Darafon A, Warkentin A, Bauer R. 3D metal removal simulation to determine uncut chip thickness, contact length, and surface finish in grinding. *International Journal of Advanced Manufacturing Technology* 2013;66:1715–24. <https://doi.org/10.1007/s00170-012-4452-1>.
- [30] Malkin S. BOOK REVIEW Grinding Technology. Theory and Applications of Machining with Abrasives. vol. 31. 1991.

[31]Hou ZB, Komanduri R. On the mechanics of the grinding process - Part I. Stochastic nature of the grinding process. *International Journal of Machine Tools and Manufacture* 2003;43:1579–93. [https://doi.org/10.1016/S0890-6955\(03\)00186-X](https://doi.org/10.1016/S0890-6955(03)00186-X).